https://doi.org/10.5194/egusphere-2026-1269
Preprint. Discussion started: 22 May 2026

GESat GEN1: In-Orbit Performance Review of a Compact SWIR Fizeau Interferometer for Facility-scale Methane Detection and Quantification

Florian Pignol[1], Sebastien Dorgan[1], Pablo Jais[1], Frédéric Romand[1], Gregoire Hein[1], Vincent Cassé[2], Raymond Armante[3], Nicolas Meilhac[4], and Cyril Crevoisier[3]

[1]Absolut Sensing, Toulouse, France
[2]Laboratoire de Météorologie Dynamique (LMD/IPSL), École des Ponts, École polytechnique, Institut polytechnique de Paris, F-91128, Palaiseau, France
[3]Laboratoire de Météorologie Dynamique (LMD/IPSL), CNRS, École polytechnique, Institut polytechnique de Paris, F-91128 Palaiseau, France
[4]Laboratoire de Météorologie Dynamique (LMD/IPSL), Polytechnique Solutions, École Polytechnique, F-91128, Palaiseau, France

Correspondence: Florian Pignol (florian.pignol2@gmail.com)

Abstract. The GESat GEN1 mission is a 16U microsatellite developed and operated by Absolut Sensing to demonstrate high-resolution methane monitoring using a compact SWIR Fizeau interferometer. GEN1 provides a 50 m ground sampling distance to monitor facility-scale methane plumes. It is rated for an average detection rate of 500 $\mathrm{kg\,h^{-1}}$, with the capacity to resolve leaks as small as 100 $\mathrm{kg\,h^{-1}}$ in pristine environmental conditions. The system is designed to achieve a column-retrieval precision of 120 ppbv, defined as the mean standard deviation of the retrieved column-averaged dry-air mole fraction of methane over operational conditions. This corresponds to a random error of approximately 6.5 % relative to a background concentration of 1850 ppbv.

The paper first presents the GEN1 mission and its interferometric payload, designed to enable selective methane sensing from a highly compact platform. It then describes the retrieval architecture, based on a physics-guided parametric algorithm that occupies an intermediate complexity between matched-filter methods, as used for missions such as Tanager-1 and EMIT (Carbon Mapper, 2024), and full physics schemes using high accuracy radiative transfer code such as libRadtran or 4A/OP (Mayer and Kylling, 2005; Scott and Chédin, 1981; Chéruy et al., 1995). The proposed model generates top-of-atmosphere radiances in the SWIR [1550, 1700nm] region with no systematic bias relative to reference full-physics model and a random error below 0.2 ppbv in methane column retrieval. Moreover, on identical computing hardware, the physics-guided parametric approach achieves a processing speed approximately 20×10^3 times faster than the full-physics model. This strategy therefore provides a balanced trade-off between robustness, accuracy, and computational cost, enabling large-scale processing compatible with constellation-level operations while preserving radiometric fidelity required for quantitative methane retrievals. Supported by this instrument and retrieval design, representative in-orbit results are reported, including methane plume detections over industrial facilities, together with an assessment of current limitations and planned evolutions of the processing chain. Finally, the paper concludes by evaluating the mission's performance against its design specifications. With more than

https://doi.org/10.5194/egusphere-2026-1269
Preprint. Discussion started: 22 May 2026

160 acquisitions processed, the system achieves an average precision of 111 ppbv, successfully meeting the mission's primary target, with an average detection sensitivity of 450 $\mathrm{kg\,h^{-1}}$. Notably, several measurements achieved precision better than 80 ppbv, which enables an ultimate methane plume detection limit corresponding to emission rates below 100 $\mathrm{kg\,h^{-1}}$ under ideal meteorological conditions. This on-orbit demonstration confirms the viability of the Fizeau interferometric approach for high-resolution monitoring and paves the way for future constellation deployment.

1 Introduction

Methane (CH_4) is the second most significant anthropogenic greenhouse gas, contributing approximately 20 % of the total radiative forcing from long-lived greenhouse gases (Kirschke et al., 2013). While its atmospheric abundance is significantly lower than that of CO_2, its Global Warming Potential is 84–86 times greater over a 20-year horizon (Jongaramrungruang et al., 2021). This high efficiency as an infrared absorber, combined with a relatively short atmospheric lifetime of approximately 9 years (Montzka et al., 2011; Prather et al., 2012; Shindell et al., 2012), makes methane mitigation one of the most effective levers for slowing near-term global warming.

Over the past decade, a multi-tiered satellite observing system for atmospheric methane has emerged, combining coarse-resolution global mappers, e.g. GOSAT (Yoshida et al., 2011), Sentinel-5P/TROPOMI (Latsch et al., 2022), and the upcoming CO2M mission (Sierk et al., 2021). However, within the anthropogenic methane sources, accounting for approximately 60 % of the total methane emissions (Saunois et al., 2020), the "super-emitters" have a disproportionate share. These include specific facility-scale point sources such as oil and gas infrastructure, coal mines, and landfills, and they produce high-rate emission events that are often stochastic and remain largely undetected by coarse-resolution global monitoring systems. To mitigate this limitation, higher-resolution imaging spectrometers such as PRISMA (Cogliati et al., 2021), EnMAP (Storch et al., 2023), EMIT, Gaofen-5B AHSI (He et al., 2024), ZY-1 AHSI (Irakulis-Loitxate et al., 2021), Tanager-1, the upcoming TANGO (Charuvil Asokan et al., 2025), and commercial systems, including GHGSat (Jervis et al., 2021), can detect and quantify plumes at tens-of-meters resolution, but their capacity, tasking flexibility, or operational cost currently restrict their use for continuous global monitoring.

Hence, despite current efforts, a capability gap remains for compact, dedicated methane imagers that can be deployed as cost-effective constellations to provide frequent, facility-scale coverage of key emitting regions. This gap is particularly acute in Europe, which currently lacks an operational high-resolution commercial constellation for methane sensing. Addressing this requires innovations in both payload miniaturization and retrieval algorithms to maximize information extraction from small-satellite platforms. The GESat GEN1 mission, initially introduced at the International Astronautical Federation in 2022 (Laurent et al., 2022), addresses this need by flying a selective SWIR interferometer on a 16U satellite platform. By targeting these localized, high-impact sources, the mission supports international mitigation frameworks such as the Copernicus Atmosphere Monitoring Service (CAMS) (Inness et al., 2019) and the International Methane Emissions Observatory (IMEO) (Randles et al., 2024).

https://doi.org/10.5194/egusphere-2026-1269
Preprint. Discussion started: 22 May 2026

GESat GEN1 mission has two primary objectives. First, to demonstrate the feasibility of methane sensing with a compact Fizeau interferometer at 50 m GSD from low Earth orbit. Second, to validate a physics-guided parametric retrieval framework that balances accuracy, robustness, and computational efficiency for large-scale processing.

Specifically, the mission aims to detect methane plumes with emission rates averaging 500 $\mathrm{kg\,h^{-1}}$, under standard observing conditions, and an ultimate detection threshold of 100 $\mathrm{kg\,h^{-1}}$ under ideal observing conditions. Following the *Common Practices for Quantifying Methane Emissions from Plumes Detected by Remote Sensing* (Worden et al., 2025), this target emission rate is directly linked to the column retrieval precision.

To derive the relationship between the minimum mass emission rate detectable, Q_{min}, and the retrieval precision of the column-averaged dry-air atmosphere mole fraction of methane, σ_{XCH4}, we employ the mass balance formulation established by Jacob et al. (2016):

$$Q_{\mathrm{min}} = \frac{M_{\mathrm{CH_4}} \cdot U \cdot W \cdot p \cdot q \cdot \sigma_{\mathrm{XCH4}}}{g \cdot M_a} \tag{1}$$

where W is the pixel size (50 m for GEN1), U is the effective wind speed, p is the surface pressure, typically 1013 hPa, g is the gravitational acceleration, and M_{CH4} and M_a are the molecular weights of methane and air, respectively.

In this framework, the detectability constant q is set to 2, following the definition of a detectable mean enhancement relative to the retrieval precision σ. For the GEN1 mission, an average detection of 500 $\mathrm{kg\,h^{-1}}$, assuming a wind speed of 2 $\mathrm{m\,s^{-1}}$, corresponds to a target random error σ_{XCH4} of 120 ppbv. Moreover, an ultimate detection limit of 100 $\mathrm{kg\,h^{-1}}$, assuming pristine wind condition, i.e. a speed of 0.5 $\mathrm{m\,s^{-1}}$, corresponds to a target random error σ_{XCH4} of 95 ppbv. Achieving this precision is a key metric for the mission's technical validation and its utility in supporting industrial leak detection and repair programs.

The paper is organized as follows. Section 2 introduces the GEN1 mission and instrument concept. Section 3 describes the radiative transfer modeling and the physics-guided parametric retrieval framework used to derive column-averaged dry-air atmosphere mole fraction of methane and emission rates. Section 4 presents first in-orbit performance results and representative plume examples. Finally, the conclusions are stated in Section 5.

2 Mission Overview and Instrument Concept

2.1 Satellite platform and orbit

GESat GEN1 is a 16U-class microsatellite with a total mass of approximately 25 kg, of which about 9 kg are allocated to the payload. The spacecraft operates in a Sun-synchronous low Earth orbit at an altitude of roughly 520 km, providing local overpass times optimized for solar-illuminated SWIR observations and a repeat cycle adapted to the monitoring of methane emission hotspots. Under typical illumination conditions (surface albedo 0.4 and solar zenith angle 22.5°), the integration time of the detector can be set to reach 70 % of its effective saturation level, corresponding to a full instrument's signal to noise ratio of $\mathrm{SNR} \approx 250$. Key mission parameters are summarized in Table 1.

https://doi.org/10.5194/egusphere-2026-1269
Preprint. Discussion started: 22 May 2026

Table 1. GESat GEN1 mission parameters.

Launch date	14 January 2025
Orbit	Sun-synchronous
Local time at descending node	10:50 UTC
Altitude	520 km
Mass	25 kg
Satellite size	$45 \times 28 \times 23\,\mathrm{cm}^3$
Payload size	$30 \times 20 \times 20\,\mathrm{cm}^3$
Ground sampling distance	50 m
Spectral range	1625–1660 nm
FWHM linewidth (Ismail et al., 2016)	1 nm
Mean free spectral range (Ismail et al., 2016)	2.58 nm / $9.6\,\mathrm{cm}^{-1}$
Detector pixel pitch	15 µm
Quantum efficiency (Q_e)	$0.75\,\mathrm{e}^-\ \mathrm{photon}^{-1}$
Dark current (I_{dc})	$91.5\,\mathrm{fA\ pixel}^{-1}\,\mathrm{s}^{-1}$
Readout noise	$60\,\mathrm{e}^-$
Instrument SNR	250

2.2 Optical payload

The GEN1 optical payload is a compact push-frame interferometric imager, optimized for methane sensing in the confined SWIR [1625, 1660 nm] window. Its architecture, illustrated in Fig. 1, consists of a three-mirror anastigmat (TMA) telescope, a fixed-path-difference Fizeau interferometer, a narrow spectral selection filter, a reimaging relay, and an InGaAs sensor focal plane. The off-axis TMA forms a low-aberration, diffraction-limited image at the interferogram plane, where a wedged Fizeau plate introduces a spatially varying optical path difference (ODP) in the along-track direction. This modulation encodes the scene radiance into a two-dimensional interferometric fringes pattern from which spectrally resolved interferograms, also known as measurement vectors in the retrieval field, are later reconstructed from the consecutive push-frames.

A compact relay then transfers the modulated field to the second focal plane while preserving spatial resolution and fringe contrast. Finally, an InGaAs detector array records the image with low noise, enabling the 50 m ground sampling distance and the methane retrieval performance required by the mission.

The telescope and focal plane assembly are designed to achieve a ground sampling distance of 50 m at nadir from the 520 km orbit while maintaining sufficient signal-to-noise ratio over a broad range of surface albedos.

https://doi.org/10.5194/egusphere-2026-1269
Preprint. Discussion started: 22 May 2026

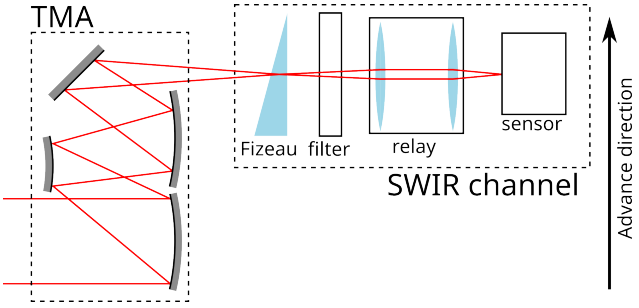

Figure 1. Schematic optical layout of the GEN1 payload, showing the TMA telescope, Fizeau interferometer, spectral filter, relay optics, and InGaAs focal plane.

2.3 Fizeau interferometer and spectral encoding

At the core of the payload is a Fizeau wedge interferometer. Compared with dispersive spectrometers, the Fizeau architecture offers a compact and mechanically robust solution well suited to small satellite platforms.

Beyond its compactness, the Fizeau configuration provides an additional advantage for methane remote sensing. In the 1.65 µm window, CH_4 absorption lines exhibit an approximately periodic spacing of $10\,\mathrm{cm}^{-1}$. This periodic structure can be purposefully matched to the spatially varying optical path difference introduced by a tailored wedge design, enhancing the encoding efficiency of methane's spectral signature without increasing system complexity.

A third advantage of the Fizeau's narrow spectral range is its relative insensitivity to interfering gases. To illustrate this, we compared the GEN1 instrument transmittance with the absorption structures of methane (CH_4), water vapour (H_2O), and carbon dioxide (CO_2) using a controlled three-gas simulation with the following conditions:

- Pressure: 1013.25–1050 hPa,
- Temperature: 275.974 K,
- Mixing ratios: H_2O = 8.2 g kg^{-1}, CO_2 = 0.6 g kg^{-1}, CH_4 = 1.02 mg kg^{-1}.

The comparison, shown in Fig. 2, leads to three conclusions:

1. The periodic methane absorption features will be aligned with the peaks in the wedge's spectral transmittance for some pixels, supporting strong CH_4 sensitivity.
2. CO_2 absorption is uncorrelated with the transmittance peaks, so it will not generate a significant signal in the interferogram.
3. Water vapour exhibits strong and isolated absorption peaks within the instrument spectral range that will generate an interferometric signal, introducing cross-sensitivities that remain modest and are later quantified to be on the order of 5 % in the retrieval analysis.

https://doi.org/10.5194/egusphere-2026-1269
Preprint. Discussion started: 22 May 2026

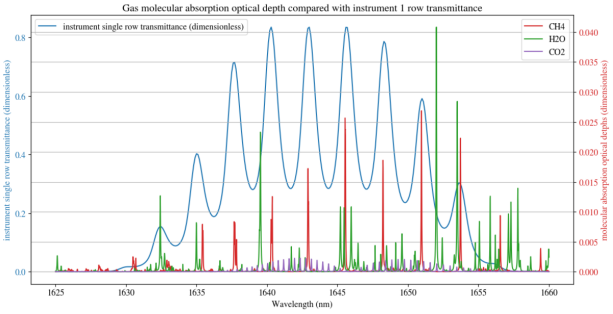

Figure 2. Comparison of instrument transmittance with the absorption optical depth of CH_4, H_2O, and CO_2 under controlled atmospheric conditions.

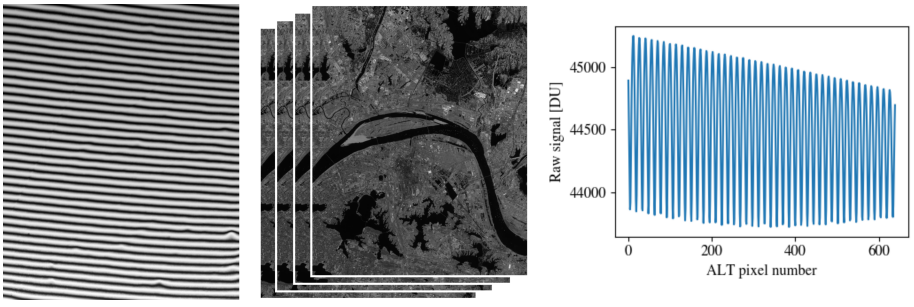

Figure 3. Illustration of the push-frame acquisition principle. Left: 2D spectral response of the instrument showing wedge-driven variations along detector rows. Center: ground scene sampled sequentially as the satellite moves. Right: interferogram for one ground cell reconstructed from successive pixel measurements.

2.4 Push-frame acquisition and image formation

GEN1 operates in a push-frame acquisition mode. As illustrated in Fig. 3, during an acquisition sequence, the spacecraft performs a pitch slew to maintain approximately constant ground-track speed on the focal plane while the detector records a series of short-exposure frames. Each ground pixel is thus observed multiple times at different positions relative to the Fizeau fringe pattern, enabling reconstruction of its interferogram by stitching the consecutive frames together. Accurate image-to-image co-registration is required to compensate for residual platform jitter and pointing drifts, ensuring that the samples contributing to a given ground pixel are correctly aligned before interferogram reconstruction. To achieve this, the processing chain employs a bundle adjustment procedure that refines the satellite's extrinsic parameters, i.e. its position and attitude, using a set of tie-points, extracted prior to optimization based on (Shi and Tomasi, 1994), providing a geometrically consistent set of poses for subpixel-accurate alignment.

https://doi.org/10.5194/egusphere-2026-1269
Preprint. Discussion started: 22 May 2026

3 Global Forward model and Retrieval Framework

3.1 Instrument Spectral Response Function

The instrument forward model links the top-of-atmosphere (TOA) radiance, at the instrument entrance, to the detected digital units (DU). Given a spectral radiance $L(\lambda)$ at the instrument entrance, the detector signal in electrons is obtained by integrating the per-wavelength electron flux over the band and exposure time.

$$N_{\mathrm{e}} = \int_{\lambda_1}^{\lambda_2} L(\lambda)\,\mathcal{R}_{\mathrm{e}}(\lambda)\,\mathrm{d}\lambda \tag{2}$$

Where $\mathcal{R}_{\mathrm{e}}$ is the instrument spectral response factor (in DU per unit spectral radiance):

$$\mathcal{R}_{\mathrm{e}}(\lambda) = g_{\mathrm{e}\to\mathrm{DU}}\,\frac{\mathcal{E}}{E_\gamma(\lambda)}\,T_{\mathrm{Fiz}}(\lambda)\,T_{\mathrm{BP}}(\lambda)\,T_{\mathrm{opt}}(\lambda)\,\mathrm{QE}(\lambda)\,t_{\mathrm{exp}}, \tag{3}$$

where $E_\gamma(\lambda) = hc/\lambda$ is the photon energy, $\mathcal{E}$ the optical étendue, $T_{\mathrm{Fiz}}(\lambda)$ the spectral element transmittance of the Fizeau described below, $T_{\mathrm{BP}}(\lambda)$ the spectral filter transmission, $T_{\mathrm{opt}}(\lambda)$ the TMA and optical relay transmission, $\mathrm{QE}(\lambda)$ the detector quantum efficiency, t_{exp} the effective integration time, and finally, digital units are obtained via the detector's conversion gain, $g_{\mathrm{e}\to\mathrm{DU}}$, that connects electrons to Digital Units.

The spectral response is strongly modulated by the Fizeau wedge that performs the interferometric encoding. Its radiometric behaviour is modelled using a scalar, multi-beam interference model. We follow the procedure of Stoykova (2005) but adapted to circular apertures instead of Gaussian beams. Under the assumptions of perfect telecentricity, an unapodized pupil without vignetting, and a slow-enough TMA, semi-analytical formulas for each successive internal reflection can be obtained.

Thus, the convergent transmittance is written as the coherent sum of M reflections, each attenuated by the surface reflectance $R = \rho^2$:

$$T_{\mathrm{Fiz}}(\lambda) = 4(1-R)^2 \left\| \sum_{p=0}^{M} R^p\, I_p(\lambda) \right\|^2, \tag{4}$$

where M is the truncation order (typically $M = 15$), and $I_p(\lambda)$ is the complex integral representing the pth multi-pass ray. The term $I_p(\lambda)$ accounts for the wavelength-dependent phase accumulated across the wedge, including the effects of refractive index, wedge angle, marginal ray geometry, and gap thickness.

3.2 Atmospheric Radiative Transfer Model

Following the approach of Lommel (1889), Chandrasekhar (1960), and later Stamnes (1986), the monochromatic specific intensity $I_\lambda^{\mathrm{tot}}(\tau_\lambda, \mu, \phi)$ in a plane-parallel, absorbing and scattering atmosphere satisfies the integro-differential radiative transfer

https://doi.org/10.5194/egusphere-2026-1269
Preprint. Discussion started: 22 May 2026

equation

$$\mu \frac{\mathrm{d}I_\lambda^{\mathrm{tot}}(\tau_\lambda,\mu,\phi)}{\mathrm{d}\tau_\lambda} = I_\lambda^{\mathrm{tot}}(\tau_\lambda,\mu,\phi) - Q(\tau_\lambda,\mu,\phi) - \frac{\omega(\tau_\lambda)}{4\pi}\int_0^{2\pi}\int_{-1}^{1} P(\tau_\lambda,\mu,\phi;\mu',\phi') \times I_\lambda^{\mathrm{tot}}(\tau_\lambda,\mu',\phi')\,\mathrm{d}\mu'\,\mathrm{d}\phi' \tag{5}$$

where μ is the cosine of the zenith angle, τ_λ the optical depth, I_λ^{tot} the total radiance, ω the single scattering albedo, P the phase function, and Q an external source term. The phase function P defines angular redistribution of scattered light.

Full-Physics Radiative Transfer Models are designed to solve the integro-differential radiative transfer equation Eq. 5. The line-by-line and layer-by-layer code 4A/OP (Dogniaux et al., 2021) models molecular absorption by utilizing spectroscopic parameters from reference databases such as GEISA (Delahaye et al., 2021) or HITRAN (Gordon et al., 2022). To account for scattering by clouds and aerosols, solvers based on the Discrete Ordinates Method, such as DISORT (Stamnes et al., 1988), are coupled with these absorption models. These tools are foundational components of scientific and operational retrieval algorithms. For instance, 4A/OP serves as the core forward radiative transfer engine for the CNES 4ARTIC processing chain utilized for the operational inversion of data from the MicroCarb mission (Pascal et al., 2017). Furthermore, 4A/OP has been selected by CNES as the reference radiative transfer model for the development of several major atmospheric missions, including the next-generation interferometer IASI-NG (Crevoisier et al., 2014) and the Franco-German MEthane Remote sensing LIdar Mission (MERLIN) (Ehret et al., 2017).

While accurate, these models are computationally intensive, making them less suitable for large-scale and cost efficient applications. As a result, alternative approaches may be considered.

Matched filtering (MF) provides a fast linear alternative to full-physics retrievals. It projects measured radiance spectra onto a predefined absorption template, yielding plume enhancement estimates relative to a reference mean spectrum. Its main strength is computational efficiency, which makes it attractive for rapid plume detection. MF nonetheless presents several limitations for quantitative gas retrieval. It relies on a linearized form of Beer-Lambert's law and therefore assumes an optically thin plume, which leads to biases when absorption becomes nonlinear. Enhancements are referenced to unit absorption spectra whose shape depends on viewing geometry, atmospheric state, and surface conditions; using generic templates can introduce $\mathrm{CH_4}$ biases of order $\pm 25\,\%$ and $\mathrm{CO_2}$ errors of several fold (Carbon Mapper, 2024). Structured surface reflectance or hydrocarbon signatures may also mimic methane features, producing false detections if not screened. Scene variability in aerosols, surface pressure, or BRDF further modifies spectral shapes in ways not represented by the MF model. Finally, MF produces relative enhancements rather than absolute columns, complicating validation and the separation of retrieval and flux-inversion errors.

3.3 Physics-guided parametric Radiative Transfer Model

To address the accuracy limitations of the matched filter method and the computational speed burden of full physics methods, Absolut Sensing developed a dedicated fast radiative transfer model. The goal is not to introduce a new radiative transfer theory,

https://doi.org/10.5194/egusphere-2026-1269
Preprint. Discussion started: 22 May 2026

but rather to define a physics-guided parametric formulation that is fast, practical, and sufficiently representative to suit GESat GEN1 objectives in methane retrieval.

We are not attempting a direct analytical solution of the integro-differential radiative transfer equation Eq. 5, but propose a parametric formulation in which the top-of-atmosphere radiance is expressed as a product of multiplicative transmittances. Its parameters can be efficiently estimated during the retrieval of concentration profiles, enabling large-scale operational applications. This strategy is designed to remain consistent with three key foundations:

1. In the limit of a pristine atmosphere without aerosols or Rayleigh scattering, the formulation reduces to the Beer-Lambert law, which represents the particular solution for pure molecular absorption.

2. Rayleigh in-scattering is modeled following Bodhaine et al. (1999), who combined updated refractive index, depolarization, and molecular density data to compute Rayleigh optical depth, and demonstrated that the in-scattering behaves as an exponential transmittance term.

3. Aerosol extinction is represented by the King-Byrne formulation (King et al., 1978), which demonstrated empirically that aerosol optical depth follows a power-law spectral dependence ($\tau_a \propto \lambda^{-\alpha}$), and thus can also be expressed as an exponential transmittance.

These last two empirical foundations demonstrate that both Rayleigh in-scattering and aerosols can be parameterized as exponential transmittances. Here, we extend this idea and propose to represent light propagation as a series of multiplicative transmittance factors, each associated with a distinct physical process (absorption, molecular out-scattering, Rayleigh in-scattering, and aerosol extinction):

$$
\begin{aligned}
I(\lambda) = I_0(\lambda)\cos(\mathrm{SZA}) & \\
\cdot R(\lambda) & \quad \text{(reflectance)} \\
\cdot T_{\text{abs}}(\lambda) & \quad \text{(absorption)} \\
\cdot T_{\text{in-scat}}(\lambda) & \quad \text{(in-scattering)} \\
\cdot T_{\text{out-scat}}(\lambda) & \quad \text{(out-scattering)} \\
\cdot T_{\text{aer}}(\lambda) & \quad \text{(aerosols)}
\end{aligned}
\tag{6}
$$

3.3.1 Reflectance

Lorente et al. (2023) showed that low-order polynomials are effective for modeling reflectance variability in methane retrieval. While polynomial functions have traditionally been used to approximate reflectance variability, we prefer to use a low-order parametric model based on Principal Component Analysis (PCA) performed on the ASTER/ECOSTRESS (Meerdink et al., 2019; Baldridge et al., 2009) reflectance database. Unlike polynomials, which are purely mathematical fits, PCA components directly reflect the dominant spectral structures observed in real reflectance data. They therefore provide a more physically

https://doi.org/10.5194/egusphere-2026-1269
Preprint. Discussion started: 22 May 2026

consistent basis for representing surface reflectance in retrieval algorithms. The surface reflectance can be expressed in a parametric PCA basis as:

$$R(\lambda) = \sum_{k=1}^{K} r_k \, \mathrm{PC}_k(\lambda) \tag{7}$$

where:

- $\mathrm{PC}_k(\lambda)$ is the k-th principal component spectrum,
- r_k is the projection coefficient (or PCA score) for the given surface spectrum,
- K is the number of components retained (typically $K \leq 4$, capturing $> 99.8\,\%$ of the reflectance variance in ASTER/E-COSTRESS).

3.3.2 Molecular absorption

Considering multiple atmospheric layers and gases, the total molecular absorption optical depth can be expressed as:

$$\tau_{\text{abs}}(\lambda) = \sum_{j=0}^{G-1} \sum_{i=0}^{L-1} \bar{\sigma}_{i,j}(\lambda) \cdot \bar{N}_{i,j} \cdot \mathrm{Lp}_i \tag{8}$$

where:

- $\tau_{\text{abs}}(\lambda)$ is the absorption optical depth (dimensionless),
- the inner sum over i represents the summation across all atmospheric layers from 0 to $L-1$,
- the outer sum over j represents the summation across all gases from 0 to $G-1$,
- $\bar{\sigma}_{i,j}(\lambda)$ is the mean absorption cross-section of species j in layer i (units: $\mathrm{m}^2\,\mathrm{mol}^{-1}$),
- $\bar{N}_{i,j}$ is the number density of species j in layer i (units: $\mathrm{mol\,m}^{-3}$),
- Lp_i is the thickness of layer i (units: m).

and the molecular absorption transmittance is:

$$T_{\text{abs}}(\lambda) = \exp\left[-\tau_{\text{abs}}(\lambda)\right] \tag{9}$$

3.3.3 Molecular in-scattering

Although the method by Bodhaine et al. (1999) to represent Rayleigh in-scattering is widely used as a benchmark, its accuracy depends on knowing the CO_2 concentration for the King correction factor, which may vary significantly in our regions of interest. To overcome this limitation, several empirical formulations have been proposed, e.g. Dutton et al. (1994), Fröhlich and Shaw (1980), Nicolet (1984). These express the Rayleigh in-scattering optical depth as a power law, We propose to use the simplest form introduced by Penndorf (1957):

$$T_{\text{in-scat}}(\lambda) = \exp\left[-\beta_1 \cdot \lambda^{-\beta_2}\right] \tag{10}$$

https://doi.org/10.5194/egusphere-2026-1269
Preprint. Discussion started: 22 May 2026

3.3.4 Molecular out-scattering

We define molecular out-scattering as the scattering of photons *out* of the sensor's line of sight by atmospheric molecules. This paper proposes an empirical parametric form which encodes two observations from the full-physics simulations: (i) its spectral fingerprint follows the molecular line structure. (ii) the out-scattering contribution in SWIR [1550, 1700 nm] is small, comparable with 0.1 % extra atmosphere. The transmittance proposed is:

$$T_{\text{out-scat}}(\lambda) = \exp\left[-P_{\text{out-scat}}(\lambda)\,\tau_{\text{abs}}(\lambda)\right] \tag{11}$$

where $P_{\text{out-scat}}(\lambda)$ is a low-degree polynomial in wavelength (usually degree ≤ 3), and $\tau_{\text{abs}}(\lambda)$ is the molecular absorption optical depth, defined in Eq. (8).

We propose to use the polynomial:

$$P_{\text{out-scat}}(\lambda) = \sum_{m=0}^{M} o_m\,(\lambda - \lambda_0)^m \qquad M \leq 3, \tag{12}$$

with λ_0 a reference wavelength and $\{o_m\}$ learned during retrieval.

3.3.5 Aerosol Optical Thickness

Absorption and scattering effects of aerosols are difficult to compute rigorously since they depend on the composition, size distribution, and vertical profile of aerosols in the atmospheric column. These properties are highly variable in space and time, influenced by both natural and anthropogenic processes. Our objective is not to characterize the aerosols themselves, but to evaluate their radiative effects through the *aerosol optical thickness* (AOT). The spectral dependence of AOT, $\tau_{\text{aer}}(\lambda)$, can be parameterized using the empirical King-Byrne formula (King et al., 1978), which extends the classical Ångström relation by introducing a wavelength-dependent coefficient.

$$\tau_{\text{aer}}(\lambda) = e^{\alpha_0}\,\lambda^{\alpha_1}\,\lambda^{\alpha_2 \ln(\lambda)} \tag{13}$$

where α_0, α_1, and α_2 are empirical coefficients to be determined during the retrieval process. This formulation has been shown (Bodhaine et al., 1999) to fit well the observed wavelength dependence of aerosol optical thickness. The corresponding aerosol transmittance is then:

$$T_{\text{aer}}(\lambda) = \exp\left[-\tau_{\text{aer}}(\lambda)\right] \tag{14}$$

3.3.6 Validation with full-physics radiative transfer

The physics-guided parametric radiative transfer model was evaluated by comparing its top-of-atmosphere radiance predictions against full-physics, line-by-line and layer-by-layer, simulations generated with *libRadtran*. The test configuration reproduces a realistic satellite viewing geometry, with the instrument located at 550 km altitude observing a surface point at 23° N, 45° E on 5 July 2018 at 11:00 UTC. Atmospheric state vectors were initialized using the Gascon 2020 profile database (NOVELTIS,

https://doi.org/10.5194/egusphere-2026-1269
Preprint. Discussion started: 22 May 2026

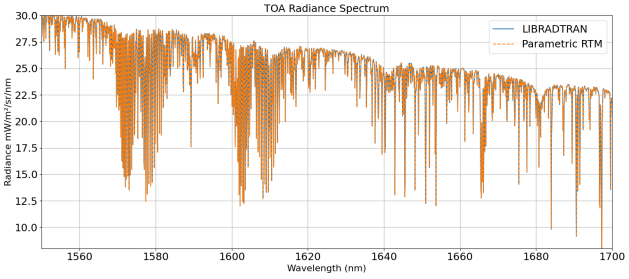

Figure 4. Top-of-atmosphere radiance from full-physics *libRadtran* simulations and the Absolut Sensing parametric model

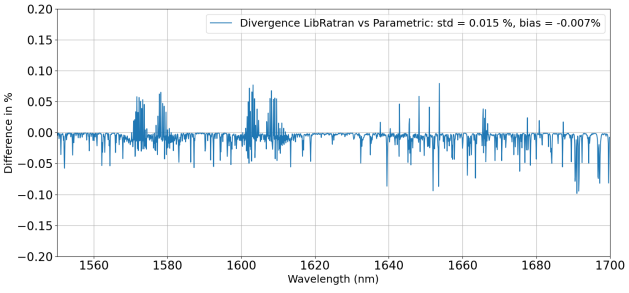

Figure 5. Difference in percent of top-of-atmosphere radiance between full-physics *libRadtran* simulations and the Absolut Sensing parametric model

2012), specifically considering H_2O, CO_2, and CH_4 as the primary absorbing species to simulate the atmospheric column. Molecular absorption cross-sections were computed from HITRAN 2020 parameters at a spectral resolution of 0.1 nm. The vertical structure of the atmosphere was discretized onto the 137 ERA5 layers (Hersbach et al., 2020), assuming clear sky cloud-free conditions. Surface boundary conditions were defined by a surface pressure of 1013.25 hPa, a temperature of 288.15 K, and a Lambertian albedo of 0.4. Solar irradiance was modeled using the Kurucz 1992 reference spectrum (Kurucz, 1994) sampled at 0.1 nm.

Figure 4 illustrates the spectral residuals between the parametric model and the *libRadtran* reference across the Short-Wave Infrared (SWIR) window (1550–1700 nm). Figure 5 exhibit high fidelity, with relative radiance differences contained within $\pm 0.1\,\%$. Statistical analysis reveals zero systematic bias and a residual 1-σ random error of 0.015 %. For the GESat GEN1 mission, this forward modeling uncertainty propagates to a methane column retrieval error of 0.011 % (0.2 ppbv). Given the mission's precision target of 120 ppbv, this modeling error is negligible. These results validate that the simplified multiplicative transmittance formulation accurately reproduces the physical processes of SWIR radiative transfer required for facility-scale methane quantification.

https://doi.org/10.5194/egusphere-2026-1269
Preprint. Discussion started: 22 May 2026

3.4 Optimal estimation formulation and theoretical performance

As we have seen, the total forward model follows a flow of transmittance and can be expressed as:

$$F(\lambda, x)[\mathrm{DU}] = g_{\mathrm{e}\to\mathrm{DU}} \cdot \int \underbrace{L_{\mathrm{TOA}}(\lambda, x)}_{\text{radiative transfer}} \underbrace{\mathcal{R}_{\mathrm{e}}(\lambda)}_{\text{ISRF}} \, \mathrm{d}\lambda \tag{15}$$

To define GESAT GEN1's state vector:

3.4.1 Gases selection.

The GEN1 interferometer samples a very narrow spectral region of 25 nm. Within this interval, only two atmospheric species imprint significant absorption features: methane (CH_4) and water vapour (H_2O). All other gases have either negligible absorption or no detectable contribution in this region.

3.4.2 Radiative effects selection.

Over a spectral window as small as 25 nm, most broadband radiative effects vary so slowly with wavelength that they can be considered spectrally constant. This includes surface albedo, broadband in-scattering, and extinction from aerosols or Rayleigh scattering. Rather than retrieving explicit parameters for each of these processes, they are collectively represented by a single multiplicative scalar factor. This factor is effectively removed by a normalization procedure applied to the measurement vector.

3.4.3 Gases Profiles selection.

Rather than retrieving independent mixing ratios for each atmospheric layer, prior vertical profiles are adopted for both species (CH_4 and H_2O). The retrieval then estimates only a multiplicative scaling factor per species, preserving the vertical structure of the profile while adjusting the column abundance.

With these simplifications, the state vector reduces to:

$$x = \left[\mathrm{XCH_4}, \mathrm{XH_2O}\right] \tag{16}$$

where XCH_4 is the column-averaged dry-air atmosphere mole fraction of methane, and XH_2O that of water vapor, which minimizes a cost function:

$$\begin{aligned} C(x,p) = &\underbrace{(F(x,\lambda_p) - M(\lambda_p))^\top S_{\mathrm{e}}^{-1} (F(x,\lambda_p) - M(\lambda_p))}_{\text{measurement mismatch}} \\ &+ \underbrace{(x - x_{\mathrm{a}})^\top S_{\mathrm{a}}^{-1} (x - x_{\mathrm{a}})}_{\text{a priori regularization}} \end{aligned} \tag{17}$$

where p represents the spectral elements of the interferogram, M the measurement, S_{e} the measurement error covariance, and S_{a} is the a priori covariance.

https://doi.org/10.5194/egusphere-2026-1269
Preprint. Discussion started: 22 May 2026

3.4.4 Ideal-Case Theoretical Performance.

Considering the Maximum A Posteriori method, also known as Optimal Estimation, Rodgers (2000) demonstrates that with the linearization $F(x) \approx F(x_a)+K(x-x_a)$ and the assumption of Gaussian priors and noise, the uncertainty (due to measurement noise and regularization by the prior), known as a posteriori covariance of the retrieved state is

$$\mathbf{S}_{\mathrm{x}} = \left(K^{\top} S_{\mathrm{e}}^{-1} K + S_{\mathrm{a}}^{-1}\right)^{-1}, \tag{18}$$

where $K = \partial F/\partial x$ is the Jacobian. In terms of the posterior standard deviation of each gas (σ_{XCH4} and σ_{XH2O}), and their Pearson correlation (ρ), $\mathbf{S}_{\mathrm{x}}$ can be expressed as:

$$\mathbf{S}_{\mathrm{x}} = \begin{bmatrix} \sigma^2_{\mathrm{XCH4}} & \rho\,\sigma_{\mathrm{XCH4}}\,\sigma_{\mathrm{XH2O}} \\ \rho\,\sigma_{\mathrm{XCH4}}\,\sigma_{\mathrm{XH2O}} & \sigma^2_{\mathrm{XH2O}} \end{bmatrix}, \tag{19}$$

Applying the above formulation of the a posteriori covariance, we evaluate the theoretical performance of the GESat GEN1 retrieval under conditions limited by photon and sensor noise (including read noise and dark current). In this analysis, the measurement quality is influenced solely by these fundamental noise sources, and σ_{XCH4} is computed for varying illumination levels and atmospheric concentrations.

Figure 6 presents σ_{XCH4}, expressed in parts per billion by volume (ppbv), as a function of the measurement vector intensity and the true CH_4 concentration. For an optimal exposure configuration, corresponding to a signal intensity of approximately 45000 DU and a background CH_4 concentration of 1850 ppbv, the combined photon and sensor noise yields a random error of approximately 60 ppbv (3.2 %). Under these conditions, the retrieval exhibits a low ρ of 5 %, demonstrating effective spectral decoupling. In short,

$$\sigma_{\mathrm{XCH4}} = 60\,\mathrm{ppbv}, \quad \sigma_{\mathrm{XH2O}} = 900\,\mathrm{ppmv}, \quad \rho = 0.05.$$

This performance significantly exceeds the GESat mission objective of 120 ppbv average precision. However, it is important to note that this 60 ppbv figure represents a "best-case" scenario. This theoretical precision assumes idealized conditions across the entire measurement chain, including optimal exposure times, nominal instrument manufacturing tolerances, and perfect calibration and characterization. Furthermore, it presupposes a fully corrected processing chain and an exhaustive knowledge of the physical state of the atmosphere (e.g., precise pressure, temperature, and aerosol profiles). In operational environments, unaccounted error and instrumental drift are expected to reduce this margin, bringing the total error budget closer to the 120 ppbv requirement.

4 On-Orbit Performance and First Results

4.1 Instrument Calibration and Corrections

The transition from the idealized theoretical precision of 60 ppbv to operational performance depends heavily on the mitigation of instrumental non-idealities that, if left uncorrected, would quickly exceed the 120 ppbv mission requirement. Therefore,

https://doi.org/10.5194/egusphere-2026-1269
Preprint. Discussion started: 22 May 2026

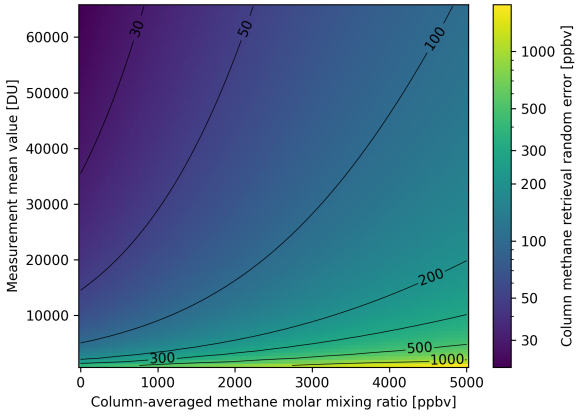

Figure 6. Posterior standard deviation of CH_4 (in ppbv) as a function of measurement vector amplitude and CH_4 concentration.

prior to interferogram reconstruction, raw Level–0 measurements are corrected for instrumental defects. Radiometric corrections include dark frame subtraction, flat field normalization, and correction of hot and dead pixels, ensuring uniform system response across the focal plane. Geometric distortions introduced by the TMA and optical relay are corrected using a polynomial distortion model, providing accurate pixel-to-ray mapping required for push-frame acquisition.

A key element of this processing stage is the calibration and correction of the spatially varying spectral response of the Fizeau interferometer. A spectral response map is derived that associates each detector pixel with its effective optical path difference and corresponding spectral weighting. This map captures both the nominal wedge-induced fringe geometry and localized manufacturing imperfections of the Fizeau interferometer. As illustrated in Fig. 7, these imperfections manifest as non-linear fringe deformations, such as bubble-like curvatures and linear streaks, which introduce irregular spectral sampling across the measurement vectors. A dedicated correction step is applied to these regions to restore a continuous and physically consistent sampling. The resulting calibrated spectral map provides the reference framework required for accurate interferogram reconstruction, ensuring that the residual errors caused by instrument mechanics remain a sub-dominant component of the total 120 ppbv error budget.

4.2 Reconstructed Interferograms

To validate the calibration and correction steps described above, reconstructed interferograms are presented using real on-orbit data acquired in push-frame mode. After radiometric, geometric, and Fizeau spectral corrections, these successive samples are combined to reconstruct a single interferogram for each ground pixel.

Figure 8 shows an example of reconstructed interferograms and the corresponding methane concentration map. The left panel presents the CH_4 map, with a background of 1850 ppbv and two localized methane emission plumes propagating westward. The plumes are centered at pixel positions $(280, 164)$ and $(154, 256)$, respectively, both are well above the instrument noise

https://doi.org/10.5194/egusphere-2026-1269
Preprint. Discussion started: 22 May 2026

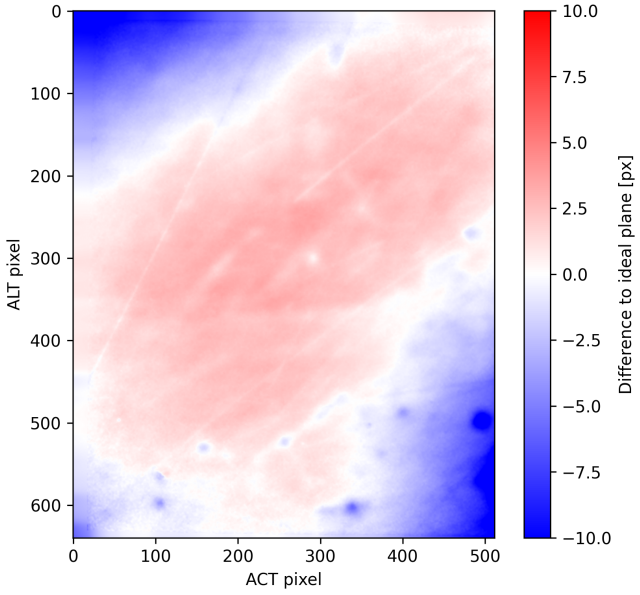

Figure 7. Examples of Fizeau interferometer imperfections observed in calibrated spectral maps: localized bubble-like curvatures and linear streaks.

level, enabling reliable detection. Two rectangles, colored red and orange, indicate two pixels either within an emission or background regions.

The right panel displays four plots, two for each rectangle. The top plots show the normalized reconstructed interferograms (red and orange) alongside the theoretical interferograms computed from the forward radiative transfer and instrument model using the estimated methane concentration. Interferograms are normalized to remove albedo dependence. The bottom plots show the residuals between reconstructed and theoretical interferograms, along with the corresponding signal-to-noise ratio (SNR).

The red pixel, located within a methane emission, exhibits a higher interferogram amplitude compared to the orange pixel in the background. This amplitude difference is a direct consequence of the higher methane concentration and allows clear detection in the CH_4 map. Both reconstructed interferograms demonstrate high fidelity to their theoretical counterparts, achieving signal-to-noise ratios (SNRs) of 176 and 172 for the source and background pixels, respectively. This performance represents only a 10–12 % reduction compared to the idealized noise-limited SNRs (199 and 190). This marginal degradation provides a snapshot of the efficacy of the Fizeau artifact corrections, radiometric calibration, and sub-pixel image-to-image alignment. While this single-example analysis confirms the local integrity of the processing chain, the following section evaluates the statistical robustness of these metrics across a global ensemble of 166 acquisitions.

These results illustrate that the GEN1 calibration and correction procedures successfully produce physically meaningful interferograms, forming a solid foundation for subsequent methane concentration retrieval and emission rate estimation.

https://doi.org/10.5194/egusphere-2026-1269
Preprint. Discussion started: 22 May 2026

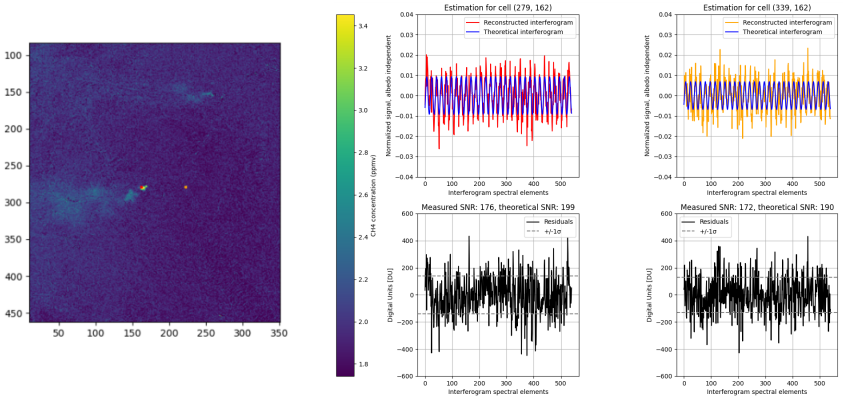

Figure 8. Left: CH_4 concentration map with two emission plumes (background 1.85 ppmv). Red and orange rectangles indicate pixels used for interferogram analysis. Right: Top: normalized reconstructed interferograms (colored) and theoretical interferograms (black) for red and orange pixels. Bottom: residuals between reconstructed and theoretical interferograms with associated SNR. The measured interferogram signal-to-noise ratio reaches about 90% of the ideal theoretical value, confirming the high fidelity of the calibration, correction, and image registration procedures.

4.3 Column methane retrieval random error

To evaluate the operational performance of the GESat GEN1 methane retrieval, global maps of column-averaged dry-air atmosphere mole fraction of methane (XCH_4) were generated from a representative set of acquisitions collected since the start of the mission. The primary mission performance metric is the retrieval precision, or column methane random error, quantified as the standard deviation of the XCH_4 estimates. This analysis encompasses 163 acquisitions distributed globally to ensure statistical significance across diverse geophysical conditions. As illustrated in Fig. 9, the dataset spans a wide range of surface types and viewing geometries, including arid deserts, urban centers, dense forests, agricultural landscapes, and coastal regions.

The XCH_4 precision is quantified by calculating the spatial standard deviation of retrieved methane concentrations over selected background regions. These regions are identified via a two-stage filtering process designed to isolate high-fidelity terrestrial pixels. First, reflectance thresholding is applied to the scene to exclude both sub-optimal low-signal surfaces (such as water bodies and shadows) and saturated pixels which are susceptible to non-linear radiometric effects and degraded signal-to-noise ratios (SNR). Second, a rigorous quality control filter is enforced based on the retrieval's information content. Pixels are discarded if their posterior standard deviation exceeds a dynamic threshold defined as three times the scene-wide median posterior uncertainty. This step ensures that the precision estimate is not skewed by ill-conditioned retrievals or unmasked clouds. Given that these filtered regions are predominantly free of localized emission plumes, we assume that 99 % of the remaining pixels constitute the atmospheric background. Under this statistical assumption, the spatial standard deviation across the 163-acquisition ensemble serves as a robust proxy for the total system random error.

https://doi.org/10.5194/egusphere-2026-1269
Preprint. Discussion started: 22 May 2026

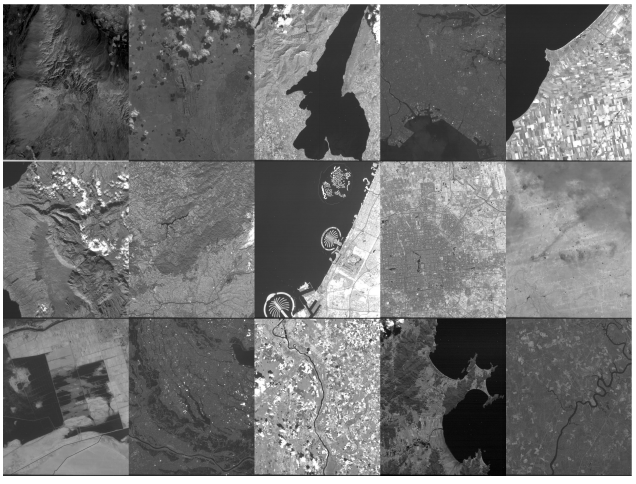

Figure 9. Subset of raw GESat GEN1 acquisitions since mission start.

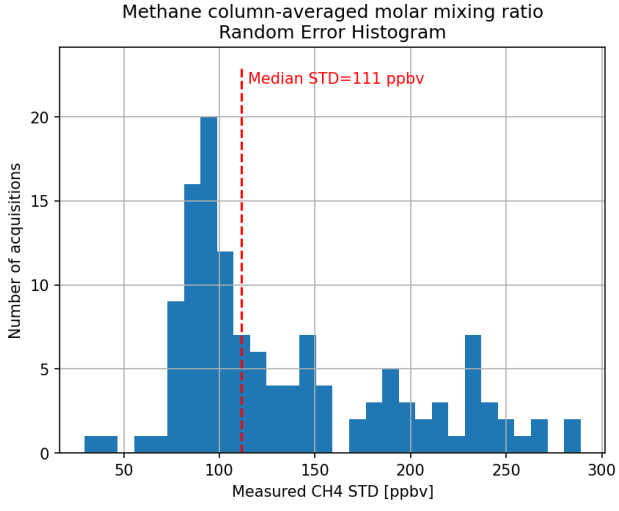

Figure 10. Measured methane concentration standard deviations in background regions.

As shown in Fig. 10, the operational average XCH_4 retrieval precision, derived from the global ensemble of 163 acquisitions, is estimated at 111 ppbv, representing a 6 % relative error against the 1850 ppbv reference background concentration. Furthermore, 25 % of the acquisitions achieved a precision below 95 ppbv, in good agreement with the GEN1 ultimate design detection limit.

While this figure exceeds the idealized theoretical precision of 60 ppbv previously discussed, the discrepancy is attributable to identifiable operational and instrumental factors. A significant portion of this additional error stems from sub-optimal exposure configurations during this first year tasking phase. The average signal intensity across the observed scenes was approxi-

https://doi.org/10.5194/egusphere-2026-1269
Preprint. Discussion started: 22 May 2026

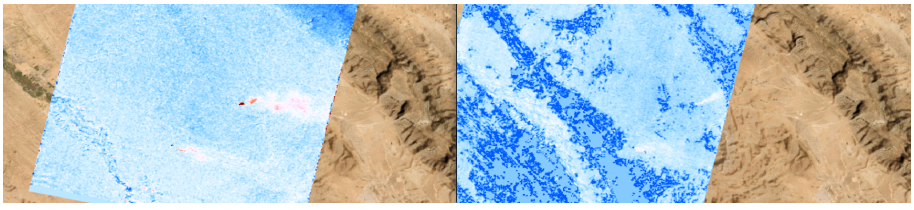

Figure 11. Revisit methane concentration maps acquired over the same site at two different times. Despite partial cloud cover in the second acquisition, pixel masking effectively suppresses false alarms. The same two methane emitters are detected in both observations, while changes in plume structure reflect differences in emission strength and wind conditions. Basemap source: ESRI.

mately 30000 DU, compared to the 45000 DU assumed in the "best-case" scenario. Adjusting the theoretical model to reflect this lower signal level yields a noise-limited precision of 85 ppbv. The remaining 30 % error margin (increasing the uncertainty from 85 ppbv to 111 ppbv) is attributed to structural residuals within the full acquisition to processing chain. These include manufacturing tolerances in the Fizeau interferometer, residual artifacts from the spectral calibration and correction maps, and sub-pixel image-to-image registration errors during the push-frame reconstruction process. Despite these operational complexities, the observed 111 ppbv precision is in excellent agreement with the GESat mission objective of 120 ppbv. As of the current mission phase, the operational processing chain consistently meets these performance requirements on average. This level of precision translates to a robust detection capability for localized methane sources with rates averaging 450 $\mathrm{kg\,h^{-1}}$. Moreover, around ten acquisitions showed a retrieval precision below 80 ppbv, enabling the detection of methane plumes with emission rates as low as 300 $\mathrm{kg\,h^{-1}}$ under favorable meteorological conditions.

4.4 Column methane retrieval stability and systematic bias

Although the primary objective of the GESat GEN1 mission is the detection and quantification of localized XCH_4 enhancements indicative of emission plumes, monitoring retrieval stability and systematic bias is critical for evaluating instrumental calibration stability, correction fidelity, and forward-model consistency.

4.4.1 Mission stability

As a first step, the stability, or internal consistency, of the column methane retrieval was assessed using 12 pairs of GESat GEN1 acquisitions over identical sites observed at different times (up to few months apart) and under varying viewing geometries and instrument configurations (Fig. 12). For each pair, the mean column methane (XCH_4) estimated from the two passes was compared. The analysis reveals a mean relative difference of 0.78 % across all sites, demonstrating a high degree of internal stability.

Residual inter-pass discrepancies are attributed to the temporal evolution of the instrumental response, uncertainties in the auxiliary atmospheric state vectors (particularly specific humidity), and natural geophysical variability. To further validate this stability, we performed a qualitative revisit analysis of specific methane-emitting facilities, as illustrated in Fig. 11. In these

https://doi.org/10.5194/egusphere-2026-1269
Preprint. Discussion started: 22 May 2026

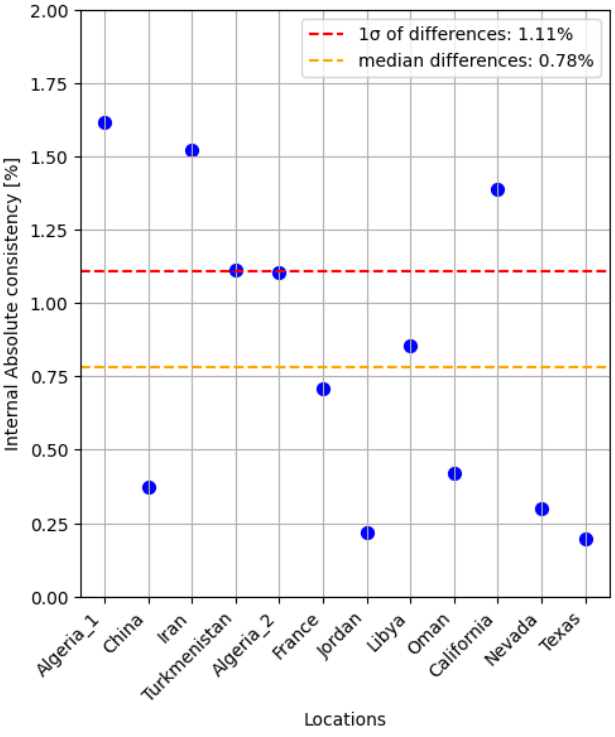

Figure 12. Internal consistency assessment using 12 acquisition pairs distributed globally. For each pair, the background methane concentration estimated from two independent passes is compared.

instances, the source locations are consistently identified across separate overpasses, with variations in plume morphology and intensity reflecting dynamic changes in emission rates and local meteorological transport. Collectively, these findings confirm the operational reliability of GESat GEN1 for high-frequency monitoring of methane point sources under diverse observational conditions.

4.4.2 Mission systematic error against TCCON, COCCON, and TROPOMI

To further characterize the systematic bias of the XCH_4 retrieval, the GESat GEN1 estimates were compared against ground-based measurements from the Total Carbon Column Observing Network (TCCON) (Wunch et al., 2011) and the Collaborative Carbon Column Observing Network (COCCON) (Frey et al., 2019), as well as satellite observations from TROPOMI. For this analysis, direct column-to-column comparisons were performed. It should be noted that these comparisons do not account for differences in the column averaging kernels, which are inherently dependent on the respective spectral ranges and sensitivities of the instruments.

A first validation study was performed in April 2025 at the Xianghe (TCCON) (Zhou et al., 2022b) and Beijing (COCCON) stations in China (Zhou et al., 2022a). This comparison utilized a single coincident GESat GEN1 acquisition and one

https://doi.org/10.5194/egusphere-2026-1269
Preprint. Discussion started: 22 May 2026

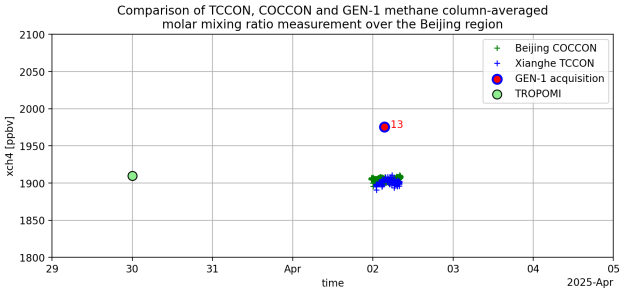

Figure 13. Validation of XCH_4 retrievals against ground-based TCCON (Xianghe) and COCCON (Beijing) measurements and TROPOMI satellite data in China (April 2025).

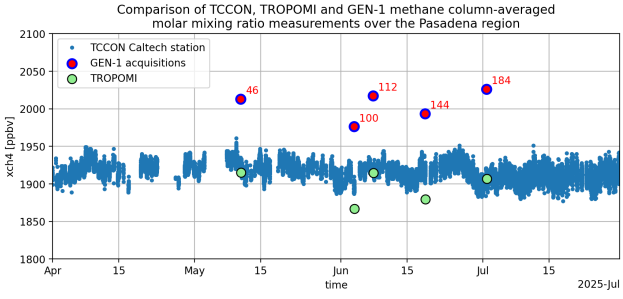

Figure 14. Validation of XCH_4 retrievals against ground-based TCCON measurements and TROPOMI satellite data over Pasadena, USA (May–July 2025).

TROPOMI overpass. As illustrated in Fig. 13, the measured XCH_4 values were 1904 ppbv for TCCON, 1907 ppbv for COCCON, and 1910 ppbv for TROPOMI. The GESat GEN1 retrieval estimated a mean concentration of 1975 ppbv. For this location, the systematic bias is +68 ppbv, or 3.6 % relative to the TCCON station.

A second validation study was conducted at the Caltech TCCON station in Pasadena, USA (Wennberg et al., 2022). Five GESat GEN1 acquisitions were collected over the site between May and July 2025, coincident with five TROPOMI overpasses. As illustrated in Fig. 14, the TCCON reference measured a mean X_{CH_4} of 1917 ± 11 ppbv. During the same period, the TROPOMI spatial average was 1897 ± 22 ppbv, while the GESat GEN1 ensemble yielded a mean concentration of 2005 ± 20 ppbv. On this site, the GESat GEN1 retrieval exhibits a systematic bias of +88 ppbv, or 4.6 % relative to the TCCON reference.

While these results indicate a consistent positive offset in the current GEN1 retrieval chain, the stability of this bias is promising for future cross-calibration efforts. Furthermore, this offset does not impede the primary mission goal of plume detection and quantification, as emission detection relies on the relative enhancement (ΔXCH_4) above the local background rather than an absolute estimation.

https://doi.org/10.5194/egusphere-2026-1269
Preprint. Discussion started: 22 May 2026

5 Conclusions

The GESat GEN1 mission represents the first european commercial mission aimed at high-resolution methane monitoring. This paper presented the on-orbit validation of its compact SWIR Fizeau interferometer in a 16U microsatellite platform. By achieving a ground sampling distance of 50 m and a measured signal-to-noise ratio (SNR) near 250, GEN1 confirms the viability of an interferometric concept specifically optimized for facility-scale methane quantification.

A first objective of the mission is the detection and quantification of methane plumes with emission rates averaging 500 $\mathrm{kg\,h^{-1}}$. To reach this threshold, a column-averaged dry-air mole fraction (XCH_4) retrieval average precision of 120 ppbv is required. Analysis of a 163-acquisition global ensemble yields an operational precision of 111 ppbv. This performance validates the mission's capability to meet its primary mandate with an average detection sensitivity of 450 $\mathrm{kg\,h^{-1}}$, providing a stable baseline for point-source monitoring.

The success of the mission relies on the unique advantages of the interferometric approach. The architecture enables a compact entrance aperture, facilitating the use of cost-effective satellite platforms, while maintaining high radiometric efficiency. By distributing spectral information across optical path differences rather than single resolution elements, the instrument integrates a larger fraction of incoming photons. Furthermore, the targeted sensitivity to methane allows for a physics-guided parametric retrieval that is 2×10^4 times faster than reference line-by-line models.

A second objective of the mission is to reach an ultimate detection limit of 100 $\mathrm{kg\,h^{-1}}$ in pristine conditions. To reach this goal, a column-averaged dry-air mole fraction (XCH_4) retrieval average precision of 95 ppbv is required. As of today, 25 % of the acquisitions reached this objective, while an encouraging result for a first year mission, we identify clear leads for future optimization:

- **Exposure Time Optimization:** Increasing average signal levels from 28000 DU toward the nominal 45000 DU would lower the noise-limited floor from 85 ppbv toward 60 ppbv.
- **Image-to-Image Alignment:** Improving sub-pixel registration during the push-frame reconstruction will reduce the 30 % error margin attributed to structural residuals.
- **Cross-Calibration:** Validation against TCCON (Pasadena, Xianghe) and COCCON (Beijing) revealed a stable systematic bias of 3.6 % to 4.2 %. While this does not impede relative plume quantification, future iterations will incorporate these offsets to improve absolute concentration accuracy.

By addressing these operational factors, reaching a retrieval precision of 90 ppbv is considered a realistic near-term target for the processing chain. Such an improvement would significantly enhance the mission's impact, lowering the methane plume average operational detection threshold to approximately 370 $\mathrm{kg\,h^{-1}}$ under standard conditions and to 95 $\mathrm{kg\,h^{-1}}$ in pristine conditions.

Overall, GEN1 establishes the interferometric push-frame concept as a scalable solution for high-resolution greenhouse gas monitoring. These results lay the foundation for a future constellation providing operational, frequent, and cost-effective global monitoring, aiming to achieve a nominal detection threshold of 100 $\mathrm{kg\,h^{-1}}$.

https://doi.org/10.5194/egusphere-2026-1269
Preprint. Discussion started: 22 May 2026

Code availability. As the retrieval code is proprietary to Absolut Sensing, we will not be making it publicly available. We have extensively described the conceptual and mathematical ideas contained in the code throughout this article.

Data availability. Example methane retrieval data are available upon request.

Author contributions. FP, SD, PJ, FR, and GH analyzed the instrument characterization and satellite data, they developed, and implemented retrieval concept. VC, RA, NM, and CC analyzed and verified the retrieval method. Florian Pignol wrote the manuscript with comments and revisions from all authors

Competing interests. The authors declare that they have no conflict of interest.

Acknowledgements. We express our gratitude to the Absolut Sensing Operations team for providing the extensive dataset from GESat GEN1 observations. Additionally, we thank the Banque Publique d'Investissement for facilitating our collaboration with the Laboratoire de Météorologie Dynamique (LMD/IPSL) during the design and data processing phases of the mission.

https://doi.org/10.5194/egusphere-2026-1269
Preprint. Discussion started: 22 May 2026

References

Baldridge, A. M., Hook, S. J., Grove, C. I., and Rivera, G.: The ASTER Spectral Library Version 2.0, Remote Sensing of Environment, 113, 711–715, https://doi.org/10.1016/j.rse.2008.11.007, 2009.

Bodhaine, B. A., Wood, N. B., Dutton, E. G., and Slusser, J. R.: On Rayleigh Optical Depth Calculations, Journal of Atmospheric and Oceanic Technology, 16, 1854–1861, https://doi.org/10.1175/1520-0426(1999)016<1854:ORODC>2.0.CO;2, 1999.

Carbon Mapper: Algorithm Theoretical Basis Document: L2b Methane and Carbon Dioxide Concentration Retrievals for Satellites, Tech. rep., Carbon Mapper, Inc., https://assets.carbonmapper.org/documents/L2B%20Algorithm%20Theoretical%20Basis%20Document_formatted_10-24-25.pdf, 2024.

Chandrasekhar, S.: Radiative Transfer, Dover Publications, New York, 1960.

Charuvil Asokan, H., Landgraf, J., Veefkind, P., Dellaert, S., and Butz, A.: Assessing the detection potential of targeting satellites for global greenhouse gas monitoring: insights from TANGO orbit simulations, Atmospheric Measurement Techniques, 18, 5247–5264, https://doi.org/10.5194/amt-18-5247-2025, 2025.

Chéruy, F., Scott, N. A., Armante, R., Tournier, B., and Chédin, A.: Contribution to the development of radiative transfer models for high spectral resolution observations in the infrared, Journal of Quantitative Spectroscopy and Radiative Transfer, 53, 597–611, https://doi.org/10.1016/0022-4073(95)00026-H, 1995.

Cogliati, S., Sarti, F., Chiarantini, L., Cosi, M., Lorusso, R., Lopinto, E., Miglietta, F., Genesio, L., Guanter, L., Damm, A., Pérez-López, S., Scheffler, D., Tagliabue, G., Panigada, C., Rascher, U., Dowling, T., Giardino, C., and Colombo, R.: The PRISMA imaging spectroscopy mission: overview and first performance analysis, Remote Sensing of Environment, 262, 112 499, https://doi.org/10.1016/j.rse.2021.112499, 2021.

Crevoisier, C., Clerbaux, C., Guidard, V., Phulpin, T., Armante, R., Barret, B., Camy-Peyret, C., Chaboureau, J.-P., Coheur, P.-F., Crépeau, L., Dufour, G., Labonnote, L., Lavanant, L., Hadji-Lazaro, J., Herbin, H., Jacquinet-Husson, N., Payan, S., Péquignot, E., Pierangelo, C., Sellitto, P., and Stubenrauch, C.: Towards IASI-New Generation (IASI-NG): impact of improved spectral resolution and radiometric noise on the retrieval of thermodynamic, chemistry and climate variables, Atmospheric Measurement Techniques, 7, 4367–4385, https://doi.org/10.5194/amt-7-4367-2014, 2014.

Delahaye, T., Armante, R., Scott, N. A., Jacquinet-Husson, N., Chédin, A., Crépeau, L., Crevoisier, C., Douet, V., Perrin, A., Barbe, A., Boudon, V., Campargue, A., Coudert, L. H., Ebert, V., Flaud, J.-M., Gamache, R. R., Jacquemart, D., Jolly, A., Kwabia-Tchana, F., Kyuberis, A., Lyulin, O. M., Manceron, L., Mikhailenko, S., Moazzen-Ahmadi, N., Müller, H. S. P., Naumenko, O. V., Nikitin, A., Perevalov, V. I., Richard, C., Starikova, E. N., Tashkun, S. A., Tyuterev, V. G., Vander Auwera, J., Vispoel, B., Yachmenev, A., and Yurchenko, S. N.: The 2020 edition of the GEISA spectroscopic database, Journal of Molecular Spectroscopy, 380, 111 510, https://doi.org/10.1016/j.jms.2021.111510, 2021.

Dogniaux, M., Crevoisier, C., Armante, R., Capelle, V., Delahaye, T., Cassé, V., De Mazière, M., Deutscher, N. M., Feist, D. G., Garcia, O. E., Griffith, D. W. T., Hase, F., Iraci, L. T., Kivi, R., Morino, I., Notholt, J., Pollard, D. F., Roehl, C. M., Shiomi, K., Strong, K., Té, Y., Velazco, V. A., and Warneke, T.: The Adaptable 4A Inversion (5AI): description and first XCO_2 retrievals from Orbiting Carbon Observatory-2 (OCO-2) observations, Atmospheric Measurement Techniques, 14, 4689–4706, https://doi.org/10.5194/amt-14-4689-2021, 2021.

Dutton, E. G., Reddy, P., Ryan, S., and DeLuisi, J. J.: Features and Effects of Aerosol Optical Depth Observed at Mauna Loa, Hawaii: 1982–1992, Journal of Geophysical Research: Atmospheres, 99, 8295–8306, https://doi.org/10.1029/93JD03520, 1994.

https://doi.org/10.5194/egusphere-2026-1269
Preprint. Discussion started: 22 May 2026

Ehret, G., Bousquet, P., Pierangelo, C., Alpers, M., Millet, B., Abshire, J. B., Bovensmann, H., Burrows, J. P., Chevallier, F., Ciais, P., Crevoisier, C., Fix, A., Flamant, P., Frankenberg, C., Gibert, F., Heim, B., Heimann, M., Houweling, S., Hubberten, H. W., Jöckel, P., Law, K., Löw, A., Marshall, J., Agusti-Panareda, A., Payan, S., Prigent, C., Rairoux, P., Sachs, T., Scholze, M., and Wirth, M.: MERLIN: A French-German Space Lidar Mission Dedicated to Atmospheric Methane, Remote Sensing, 9, 1052, https://doi.org/10.3390/rs9101052, 2017.

Frey, M., Sha, M. K., Hase, F., Kiel, M., Blumenstock, T., Harig, R., Surawicz, G., Deutscher, N. M., Shiomi, K., Franklin, J. E., Bösch, H., Chen, J., Grutter, M., Ohyama, H., Sun, Y., Butz, A., Mengistu Tsidu, G., Ene, D., Wunch, D., Cao, Z., Garcia, O., Ramonet, M., Vogel, F., and Orphal, J.: Building the COllaborative Carbon Column Observing Network (COCCON): Long-term stability and ensemble performance of the EM27/SUN Fourier transform spectrometer, Atmospheric Measurement Techniques, 12, 1513–1530, https://doi.org/10.5194/amt-12-1513-2019, 2019.

Fröhlich, C. and Shaw, G. E.: New determination of Rayleigh scattering in the terrestrial atmosphere, Applied Optics, 19, 1773–1775, https://doi.org/10.1364/AO.19.001773, 1980.

Gordon, I., Rothman, L., Hargreaves, R., Hashemi, R., Karlovets, E., Skinner, F., Conway, E., Hill, C., Kochanov, R., Tan, Y., Wcisło, P., Finenko, A., Nelson, K., Bernath, P., Birk, M., Boudon, V., Campargue, A., Chance, K., Coustenis, A., Drouin, B., Flaud, J., Gamache, R., Hodges, J., Jacquemart, D., Mlawer, E., Nikitin, A., Perevalov, V., Rotger, M., Tennyson, J., Toon, G., Tran, H., Tyuterev, V., Adkins, E., Baker, A., Barbe, A., Canè, E., Császár, A., Dudaryonok, A., Egorov, O., Fleisher, A., Fleurbaey, H., Foltynowicz, A., Furtenbacher, T., Harrison, J., Hartmann, J., Horneman, V., Huang, X., Karman, T., Karns, J., Kassi, S., Kleiner, I., Kofman, V., Kwabia–Tchana, F., Lavrentieva, N., Lee, T., Long, D., Lukashevskaya, A., Lyulin, O., Makhnev, V., Matt, W., Massie, S., Melosso, M., Mikhailenko, S., Mondelain, D., Müller, H., Naumenko, O., Perrin, A., Polyansky, O., Raddaoui, E., Raston, P., Reed, Z., Rey, M., Richard, C., Tóbiás, R., Sadiek, I., Schwenke, D., Starikova, E., Sung, K., Tamassia, F., Tashkun, S., Vander Auwera, J., Vasilenko, I., Vigasin, A., Villanueva, G., Vispoel, B., Wagner, G., Yachmenev, A., and Yurchenko, S.: The HITRAN2020 molecular spectroscopic database, Journal of Quantitative Spectroscopy and Radiative Transfer, 277, 107 949, https://doi.org/10.1016/j.jqsrt.2021.107949, 2022.

He, Z., Gao, L., Liang, M., and Zeng, Z.-C.: A survey of methane point source emissions from coal mines in Shanxi province of China using AHSI on board Gaofen-5B, Atmospheric Measurement Techniques, 17, 2937–2956, https://doi.org/10.5194/amt-17-2937-2024, 2024.

Hersbach, H., Bell, B., Berrisford, P., Hirahara, S., Horányi, A., Muñoz-Sabater, J., Nicolas, J., Peubey, C., Radu, R., Schepers, D., Simmons, A., Soci, C., Abdalla, S., Abellan, X., Balsamo, G., Bechtold, P., Biavati, G., Bidlot, J., Bonavita, M., De Chiara, G., Dahlgren, P., Dee, D., Diamantakis, M., Dragani, R., Flemming, J., Forbes, R., Fuentes, M., Geer, A., Haimberger, L., Healy, S., Hogan, R. J., Hólm, E., Janisková, M., Keeley, S., Laloyaux, P., Lopez, P., Lupu, C., Radnoti, G., de Rosnay, P., Rozum, I., Vamborg, F., Villaume, S., and Thépaut, J.-N.: The ERA5 global reanalysis, Quarterly Journal of the Royal Meteorological Society, 146, 1999–2049, https://doi.org/10.1002/qj.3803, 2020.

Inness, A., Ades, M., Agustí-Panareda, A., Barré, J., Benedictow, A., Blechschmidt, A.-M., Dominguez, J. J., Engelen, R., Eskes, H., Flemming, J., Huijnen, V., Jones, L., Kipling, Z., Massart, S., Parrington, M., Peuch, V.-H., Razinger, M., Remy, S., Schulz, M., and Suttie, M.: The CAMS reanalysis of atmospheric composition, Atmospheric Chemistry and Physics, 19, 3515–3556, https://doi.org/10.5194/acp-19-3515-2019, 2019.

Irakulis-Loitxate, I., Guanter, L., Liu, Y.-N., Varon, D. J., Maasakkers, J. D., Zhang, Y., Chulakadabba, A., Wofsy, S. C., Thorpe, A. K., Duren, R. M., Frankenberg, C., Lyon, D. R., Hmiel, B., Cusworth, D. H., Zhang, Y., Segl, K., Gorroño, J., Sánchez-García, E., Sulprizio, M. P., Cao, K., Zhu, H., Liang, J., Li, X., Aben, I., and Jacob, D. J.: Satellite-based survey of extreme methane emissions in the Permian basin, Science Advances, 7, eabf4507, https://doi.org/10.1126/sciadv.abf4507, 2021.

https://doi.org/10.5194/egusphere-2026-1269
Preprint. Discussion started: 22 May 2026

Ismail, N., Kores, C. C., Geskus, D., and Pollnau, M.: Fabry–Perot resonator: spectral line shapes, generic and related Airy distributions, linewidths, finesses, and performance at low or frequency-dependent reflectivity, Optics Express, 24, 16 366–16 389, https://doi.org/10.1364/OE.24.016366, 2016.

Jacob, D. J., Turner, A. J., Maasakkers, J. D., Sheng, J., Sun, K., Liu, X., Chance, K., Aben, I., McKeever, J., and Frankenberg, C.: Satellite observations of atmospheric methane and their value for quantifying methane emissions, Atmospheric Chemistry and Physics, 16, 14 371–14 396, https://doi.org/10.5194/acp-16-14371-2016, 2016.

Jervis, D., McKeever, J., Durak, B. O. A., Sloan, J. J., Gains, D., Varon, D. J., Ramier, A., Strupler, M., and Tarrant, E.: The GHGSat-D imaging spectrometer: high-resolution methane monitoring from a small satellite, Atmospheric Measurement Techniques, 14, 2127–2140, https://doi.org/10.5194/amt-14-2127-2021, 2021.

Jongaramrungruang, S., Matheou, G., Thorpe, A. K., Zeng, Z.-C., and Frankenberg, C.: Remote sensing of methane plumes: instrument tradeoff analysis for detecting and quantifying local sources at global scale, Atmospheric Measurement Techniques, 14, 7999–8017, https://doi.org/10.5194/amt-14-7999-2021, 2021.

King, M. D., Byrne, D. M., Herman, B. M., and Reagan, J. A.: Aerosol Size Distributions Obtained by Inversions of Spectral Optical Depth Measurements, Journal of the Atmospheric Sciences, 35, 2153–2167, https://doi.org/10.1175/1520-0469(1978)035<2153:ASDOBI>2.0.CO;2, 1978.

Kirschke, S., Bousquet, P., Ciais, P., Saunois, M., Canadell, J. G., Dlugokencky, E. J., Bergamaschi, P., Bergmann, D., Blake, D. R., Bruhwiler, L., Cameron-Smith, P., Castaldi, S., Chevallier, F., Feng, L., Fraser, A., Heimann, M., Hodson, E. L., Houweling, S., Josse, B., Fraser, P. J., Krummel, P. B., Lamarque, J.-F., Langenfelds, R. L., Le Quéré, C., Naik, V., O'Doherty, S., Palmer, P. I., Pison, I., Plummer, D., Poulter, B., Prinn, R. G., Rigby, M., Ringeval, B., Santini, M., Schmidt, M., Shindell, D. T., Simpson, I. J., Spahni, R., Steele, L. P., Strode, S. A., Sudo, K., Szopa, S., van der Werf, G. R., Voulgarakis, A., van Weele, M., Weiss, R. F., Williams, J. E., and Zeng, G.: Three decades of global methane sources and sinks, Nature Geoscience, 6, 813–823, https://doi.org/10.1038/ngeo1955, 2013.

Kurucz, R. L.: Synthetic Infrared Spectra, in: Symposium - International Astronomical Union, vol. 154, pp. 523–531, https://doi.org/10.1017/S0074180900124805, 1994.

Latsch, M., Richter, A., Eskes, H., Sneep, M., Wang, P., Veefkind, P., Lutz, R., Loyola, D., Argyrouli, A., Valks, P., Wagner, T., Sihler, H., van Roozendael, M., Theys, N., Yu, H., Siddans, R., and Burrows, J. P.: Intercomparison of Sentinel-5P TROPOMI cloud products for tropospheric trace gas retrievals, Atmospheric Measurement Techniques, 15, 6257–6279, https://doi.org/10.5194/amt-15-6257-2022, 2022.

Laurent, T., Le Coarer, E., and Hurot, T.: GESat constellation: fighting climate change by measuring methane emissions from space, in: Proceedings of the 73rd International Astronautical Congress (IAC 2022), https://iafastro.directory/iac/archive/browse/IAC-22/B1/6/71388/, paper ID: 71388, 2022.

Lommel, E.: Die Photometrie der diffusen Zurückwerfung, Annalen der Physik, 272, 473–502, https://doi.org/10.1002/andp.18892720211, 1889.

Lorente, A., Borsdorff, T., Martinez-Velarte, M. C., and Landgraf, J.: Accounting for surface reflectance spectral features in TROPOMI methane retrievals, Atmospheric Measurement Techniques, 16, 1597–1608, https://doi.org/10.5194/amt-16-1597-2023, 2023.

Mayer, B. and Kylling, A.: Technical note: The libRadtran software package for radiative transfer calculations – description and examples of use, Atmospheric Chemistry and Physics, 5, 1855–1877, https://doi.org/10.5194/acp-5-1855-2005, 2005.

Meerdink, S. K., Hook, S. J., Roberts, D. A., and Abbott, E. A.: The ECOSTRESS spectral library version 1.0, Remote Sensing of Environment, 230, 111 196, https://doi.org/10.1016/j.rse.2019.05.015, 2019.

https://doi.org/10.5194/egusphere-2026-1269
Preprint. Discussion started: 22 May 2026

Montzka, S. A., Krol, M., Dlugokencky, E., Hall, B., Jöckel, P., and Lelieveld, J.: Small interannual variability of global atmospheric hydroxyl, Science, 331, 67–69, https://doi.org/10.1126/science.1197640, 2011.

Nicolet, M.: On the molecular scattering in the terrestrial atmosphere: An empirical formula for its calculation in the homosphere, Planetary and Space Science, 32, 1467–1468, https://doi.org/10.1016/0032-0633(84)90089-8, 1984.

NOVELTIS: 4A/OP Radiative Transfer Model – User Guide, Tech. Rep. NOV-3049-NT-1178 v4.3, NOVELTIS, https://4aop.noveltis.fr/wp-content/uploads/2021/08/NOV-3049-NT-1178v4.3.pdf, 2012.

Pascal, V., Buil, C., Loesel, J., Tauziede, L., Jouglet, D., and Buisson, F.: An improved microcarb dispersive instrumental concept for the measurement of greenhouse gases concentration in the atmosphere, in: International Conference on Space Optics–ICSO 2014, edited by Sodnik, Z., Cugny, B., and Karafolas, N., vol. 10563, pp. 1028–1036, https://doi.org/10.1117/12.2304219, 2017.

Penndorf, R.: Tables of the Refractive Index for Standard Air and the Rayleigh Scattering Coefficient for the Spectral Region between 0.2 and 20.0 μ and Their Application to Atmospheric Optics, J. Opt. Soc. Am., 47, 176–182, https://doi.org/10.1364/JOSA.47.000176, 1957.

Prather, M. J., Holmes, C. D., and Hsu, J.: Reactive greenhouse gas scenarios: Systematic exploration of uncertainties and the role of atmospheric chemistry, Geophysical Research Letters, 39, L09 803, https://doi.org/10.1029/2012GL051440, 2012.

Randles, C., Zavala-Araiza, D., Baranski, M., Calcan, A., Cifarelli, C., Demeter, M., France, J., Guanter, L., Irakulis-Loitxate, I., Watine-Guiu, M., Schwietzke, S., Caltigirone, M., and Hamburg, S.: The International Methane Emissions Observatory (IMEO): Integration of methane data across scales for policy-relevant results, EGU General Assembly 2024, EGU24, 16 432, https://doi.org/10.5194/egusphere-egu24-16432, 2024.

Rodgers, C. D.: Inverse Methods for Atmospheric Sounding: Theory and Practice, vol. 2 of *Series on Atmospheric, Oceanic and Planetary Physics*, World Scientific Publishing, https://doi.org/10.1142/3171, 2000.

Saunois, M., Stavert, A. R., Poulter, B., Bousquet, P., Canadell, J. G., Jackson, R. B., Raymond, P. A., Dlugokencky, E. J., Houweling, S., Patra, P. K., Ciais, P., Arora, V. K., Bastviken, D., Bergamaschi, P., Blake, D. R., Brailsford, G., Bruhwiler, L., Carlson, K. M., Carrol, M., Castaldi, S., Chandra, N., Crevoisier, C., Crill, P. M., Covey, K., Curry, C. L., Etiope, G., Frankenberg, C., Gedney, N., Hegglin, M. I., Höglund-Isaksson, L., Hugelius, G., Ishizawa, M., Ito, A., Janssens-Maenhout, G., Jensen, K. M., Joos, F., Kleinen, T., Krummel, P. B., Langenfelds, R. L., Laruelle, G. G., Liu, L., Machida, T., Maksyutov, S., McDonald, K. C., McNorton, J., Miller, P. A., Melton, J. R., Morino, I., Müller, J., Murguia-Flores, F., Naik, V., Niwa, Y., Noce, S., O'Doherty, S., Parker, R. J., Peng, C., Peng, S., Peters, G. P., Prigent, C., Prinn, R., Ramonet, M., Regnier, P., Riley, W. J., Rosentreter, J. A., Segers, A., Simpson, I. J., Shi, H., Smith, S. J., Steele, L. P., Thornton, B. F., Tian, H., Tohjima, Y., Tubiello, F. N., Tsuruta, A., Viovy, N., Voulgarakis, A., Weber, T. S., van Weele, M., van der Werf, G. R., Weiss, R. F., Worthy, D., Wunch, D., Yin, Y., Yoshida, Y., Zhang, W., Zhang, Z., Zhao, Y., Zheng, B., Zhu, Q., Zhu, Q., and Zhuang, Q.: The Global Methane Budget 2000–2017, Earth System Science Data, 12, 1561–1623, https://doi.org/10.5194/essd-12-1561-2020, 2020.

Scott, N. A. and Chédin, A.: A fast line-by-line method for atmospheric absorption computations: The Automatized Atmospheric Absorption Atlas, Journal of Applied Meteorology and Climatology, 20, 802–812, https://doi.org/10.1175/1520-0450(1981)020<0802:AFLBLM>2.0.CO;2, 1981.

Shi, J. and Tomasi, C.: Good Features to Track, in: Proceedings of the IEEE Conference on Computer Vision and Pattern Recognition (CVPR), pp. 593–600, https://doi.org/10.1109/CVPR.1994.323794, 1994.

Shindell, D., Kuylenstierna, J. C., Vignati, E., Van Dingenen, R., Amann, M., Klimont, Z., Anenberg, S. C., Muller, N., Janssens-Maenhout, G., Raes, F., Schwartz, J., Faluvegi, G., Pozzoli, L., Kupiainen, K., Höglund-Isaksson, L., Emberson, L., Streets, D., Ramanathan, V.,

https://doi.org/10.5194/egusphere-2026-1269
Preprint. Discussion started: 22 May 2026

Hicks, K., Oanh, N. T., Milly, G., Williams, M., Demkine, V., and Fowler, D.: Simultaneously mitigating near-term climate change and improving human health and food security, Science, 335, 183–189, https://doi.org/10.1126/science.1210026, 2012.

Sierk, B., Fernandez, V., Bézy, J.-L., Meijer, Y., Durand, Y., Bazalgette Courrèges-Lacoste, G., Pachot, C., Löscher, A., Nett, H., Minoglou, K., Boucher, L., Windpassinger, R., Pasquet, A., Serre, D., and Te Hennepe, F.: The Copernicus CO2M mission for monitoring anthropogenic carbon dioxide emissions from space, in: International Conference on Space Optics – ICSO 2020, https://doi.org/10.1117/12.2599613, 2021.

Stamnes, K.: The Theory of Multiple Scattering of Radiation in Plane Parallel Atmospheres, Reviews of Geophysics, 24, 299–310, https://doi.org/10.1029/RG024i002p00299, 1986.

Stamnes, K., Tsay, S.-C., Wiscombe, W., and Jayaweera, K.: Numerically stable algorithm for discrete-ordinate-method radiative transfer in multiple scattering and emitting layered media, Applied Optics, 27, 2502–2509, https://doi.org/10.1364/AO.27.002502, 1988.

Storch, T., Honold, H.-P., Chabrillat, S., Habermeyer, M., Tucker, P., Brell, M., Ohndorf, A., Wirth, K., Betz, M., Kuchler, M., Mühle, H., Carmona, E., Baur, S., Mücke, M., Löw, S., Schulze, D., Zimmermann, S., Lenzen, C., Wiesner, S., Aida, S., Kahle, R., Willburger, P., Hartung, S., Dietrich, D., Plesia, N., Tegler, M., Schork, K., Alonso, K., Marshall, D., Gerasch, B., Schwind, P., Pato, M., Schneider, M., de los Reyes, R., Langheinrich, M., Wenzel, J., Bachmann, M., Holzwarth, S., Pinnel, N., Guanter, L., Segl, K., Scheffler, D., Foerster, S., Bohn, N., Bracher, A., Soppa, M. A., Gascon, F., Green, R., Kokaly, R., Moreno, J., Ong, C., Sornig, M., Wernitz, R., Bagschik, K., Reintsema, D., La Porta, L., Schickling, A., and Fischer, S.: The EnMAP imaging spectroscopy mission towards operations, Remote Sensing of Environment, 294, 113 632, https://doi.org/10.1016/j.rse.2023.113632, 2023.

Stoykova, E.: Transmission of a Gaussian beam by a Fizeau interferential wedge, Journal of the Optical Society of America A, 22, 2756–2765, https://doi.org/10.1364/JOSAA.22.002756, 2005.

Wennberg, P. O., Roehl, C., Wunch, D., Blavier, J.-F., Toon, G. C., Allen, N. T., Treffers, R., and Laughner, J.: TCCON data from Caltech (US), Release GGG2020.R0, https://doi.org/10.14291/tccon.ggg2020.pasadena01.R0, 2022.

Worden, J., Green, P., Eldering, A., and Sherwin, E.: Common Practices for Quantifying Methane Emissions from Plumes Detected by Remote Sensing, NIST Interagency Report (IR) NIST.IR.857, National Institute of Standards and Technology, https://doi.org/10.6028/NIST.IR.8575, 2025.

Wunch, D., Toon, G. C., Blavier, J.-F. L., Washenfelder, R. A., Notholt, J., Connor, B. J., Griffith, D. W. T., Sherlock, V., and Wennberg, P. O.: The Total Carbon Column Observing Network, Philosophical Transactions of the Royal Society A: Mathematical, Physical and Engineering Sciences, 369, 2087–2112, https://doi.org/10.1098/rsta.2010.0240, 2011.

Yoshida, Y., Ota, Y., Eguchi, N., Kikuchi, N., Nobuta, K., Tran, H., Morino, I., and Yokota, T.: Retrieval algorithm for CO_2 and CH_4 column abundances from short-wavelength infrared spectral observations by the Greenhouse gases Observing Satellite, Atmospheric Measurement Techniques, 4, 717–734, https://doi.org/10.5194/amt-4-717-2011, 2011.

Zhou, M., Ni, Q., Cai, Z., Langerock, B., Nan, W., Yang, Y., Che, K., Yang, D., Wang, T., Liu, Y., and Wang, P.: CO_2 in Beijing and Xianghe Observed by Ground-Based FTIR Column Measurements and Validation to OCO-2/3 Satellite Observations, Remote Sensing, 14, 3769, https://doi.org/10.3390/rs14153769, 2022a.

Zhou, M., Wang, P., Kumps, N., Hermans, C., and Nan, W.: TCCON data from Xianghe, China, Release GGG2020.R0, https://doi.org/10.14291/TCCON.GGG2020.XIANGHE01.R0, 2022b.